materials

MDPI

Article

Study of Ce, Ca, Fe, and Mn-Doped $LaCoO_3$ Perovskite Oxide for the Four-Way Purification of PM, NO_x, CO, and HC from Diesel Engine Exhaust

Yinghui Wang [1,2], Xiurong Guo [1,*], Danfeng Du [3] and Shaochi Yang [1]

[1] Mechanical and Electrical Engineering Institute, Northeast Forestry University, Harbin 150040, China; sjidan@163.com (Y.W.); sc_yang_97@163.com (S.Y.)
[2] School of Electrical Engineering, Sui Hua University, Suihua 152061, China
[3] Transportation College, Northeast Forestry University, Harbin 150040, China; dudfeng@nefu.edu.cn
* Correspondence: wangyinghui@nefu.edu.cn

Abstract: Perovskite-type catalysts were widely used in the field of automobile exhaust purification due to their inherent physicochemical properties and excellent doping characteristics. A series of $La_{1-x}M_xCo_{1-y}N_yO_3$ (M = Ce, Ca; N = Fe, Mn) perovskite-type catalyst samples were prepared by sol-gel method for the four-way purification of PM, NO_x, CO, and HC emitted by diesel exhaust. The activity of catalyst samples was tested by simulation experiments and hydrogen temperature-programmed reduction (H_2-TPR). Catalyst samples were characterized by means of XRD, FT-IR, SEM, BET, and XPS analysis. The results demonstrated that the perovskite-type catalyst samples with a particle pore size of 3–5 μm can be prepared by sol-gel method. When A-site of $LaCoO_3$ perovskite-type oxide was doped by cerium ions, the catalyst samples produced small distortion. The doping of cerium ions to A-site was more conducive to the four-way purification of diesel exhaust than calcium ions. $La_{0.8}Ce_{0.2}CoO_3$ perovskite-type samples showed the best purification efficiency, and the purification efficiencies of PM, NO_x, CO, and HC were 90%, 85%, 94%, and 100%, respectively. When the B-site of $La_{0.8}Ce_{0.2}CoO_3$ perovskite was doped with iron ions, the purification efficiency of catalyst samples for PM and NO_x can be further enhanced. When the B-site of $La_{0.8}Ce_{0.2}CoO_3$ perovskite was doped with manganese ions, the purification efficiency of the catalyst samples for PM can be further enhanced. It can be seen from the simulation experiments that $La_{0.8}Ce_{0.2}Co_{0.7}Fe_{0.3}O_3$ perovskite was the best doping amount, and the purification efficiencies of PM, NO_x, CO, and HC were 95%, 92%, 94%, and 100%, respectively.

Keywords: perovskite-type catalyst; diesel exhaust; sol-gel method; four-way purification; doping amount

Citation: Wang, Y.; Guo, X.; Du, D.; Yang, S. Study of Ce, Ca, Fe, and Mn-Doped $LaCoO_3$ Perovskite Oxide for the Four-Way Purification of PM, NO_x, CO, and HC from Diesel Engine Exhaust. *Materials* **2022**, *15*, 4149. https://doi.org/10.3390/ma15124149

Academic Editors: Dominique Agustin and Jana Pisk

Received: 7 May 2022
Accepted: 7 June 2022
Published: 10 June 2022

1. Introduction

The pollutants emitted by diesel exhaust mainly include particulate matter (PM), nitrogen oxides (NO_x), carbon monoxide (CO), and hydrocarbons (HC) [1]. Among them, the micron PM emitted from diesel engine is an important factor causing haze weather, which can seriously damage the human respiratory system, and even lead to the increase of lung cancer incidence rate. NO_x emission is the main cause of acid rain. The combination of CO and human hemoglobin will cause headache, syncope, and even endanger human life. HC causes serious damage to the human respiratory, nervous, and hematopoietic systems, which mixed with NO_x under light conditions may form photochemical smog [2–4]. Since this century, the application research of perovskite-type catalysts in the field of engine aftertreatment technology has been rapidly developed, reasonable doping and modification of perovskite-type catalysts can effectively purify the pollutants emitted by engine [5,6]. Hong Wang et al. [7] prepared three kinds of different perovskite-type catalysts by combining sol-gel method and impregnation method. The XRD and SEM characterization results proved that the catalysts can be uniformly supported on the zeolite

surface. The substitution of La^{3+} at the A site by Cs^{+} can enhance the catalytic activity of the catalysts. Xuelei Mei et al. [8] synthesized the double perovskite-type $La_2NiB'O_6$ catalyst material with a three-dimensional ordered macroporous structure successfully by crystal template method. The purification efficiency and catalytic activity of $LaNiO_3$ on PM can be improved by doping the B site with manganese, iron, cobalt, and copper ions, respectively. When the molar ratio of cobalt ions to nickel ions is 1:1, the purification efficiency of La_2NiCoO_6 on PM can reach 98.2%. Shiva Abedi et al. [9] synthesized $LaFeO_3$, $LaFe_{0.7}Mn_{0.3}O_3$, and $LaMn_{0.7}Fe_{0.3}O_3$ nano-scale perovskite-type catalysts with different doping amount by sol-gel method, the CO was used as a reducing agent to selectively reduce NO through simulation experiments, in addition to studying the function of synthesized catalysts and finding the optimal catalyst in the CO-SCR process by XRD, SEM characterization methods, and chemical reaction kinetic model. The results showed that the conversion efficiency of CO and NO increased with the synergistic effect of manganese ions and iron ions. When the stoichiometry of iron and manganese ions were 0.3 and 0.7, respectively, the catalyst activity can reach the highest, and the conversion efficiency of CO and NO improved with the increase of reaction temperature and decrease of space velocity. Fan Fang et al. [10] synthesized porous perovskite-type $La_{0.6}Sr_{0.4}CoO_{3-\delta}$ nanotubes by sol-gel method combined with electrospinning technique following the calcination, which were treated with nitric acid to obtain a catalyst with a larger specific surface area. The catalysts were tested by temperature-programmed experiments. The results showed that the catalytic activity of $La_{0.6}Sr_{0.4}CoO_{3-\delta}$ nanotubes for PM was positively correlated with its specific surface area. The research team also analyzed the specific purification mechanism. Jiang, Q et al. [11] doped the A site and B site of $LaNiO_3$ perovskite with calcium and copper ions, respectively, and detailed the effect of different doping amount on the physicochemical structure of the catalyst materials, revealed that the doped perovskite-type catalysts can effectively promote O^{2-} transport during the redox reaction of HC, and can be used as an effective carrier for O_{ads} in the low-temperature oxidation reaction, while decreasing the activation temperature of the overall reaction. E. Magnone et al. [12] studied the effects of different synthesis methods of $La_{0.6}Sr_{0.4}CoO_{3-\delta}$ powder on the adsorption and desorption of oxygen, particle size, specific surface area of the catalytic materials, the results showed that different synthesis methods directly affect the particle size and specific surface area of the catalysts, and indirectly affect the adsorption and desorption capacity of the catalysts for oxygen. Long Tang et al. [13] prepared $LaKCoO_3/\gamma\text{-}Al_2O_3$/cordierite catalysts by a two-step impregnation method. The porous structure of $\gamma\text{-}Al_2O_3$ can evenly distribute $LaKCoO_3$ on the surface of cordierite, and obtain a high specific surface area, thermal stability, and catalytic activity. When the reaction temperature is 390 °C, the conversion rate of $LaKCoO_3/\gamma\text{-}Al_2O_3$/cordierite catalyst for soot particles can reach 90%, and the CO_2 selectivity is 99.8%. Siran Zhang et al. [14] proposed a method of constructing highly dispersed Pt and oxygen vacancies on the catalysts. The $LaCo_xNi_{0.87-x}Pt_{0.13}O_3$ perovskite-type catalyst was supported on SiO_2 by the citric acid method and the impregnation method. Under low-temperature conditions, the $LaCo_xNi_{1-x}O_3$ surface can form high-dispersion double active centers, namely Pt clusters and O vacancies, which showed significant activity for CO oxidation.

Although the diesel engine exhaust purification technology by perovskite-type catalysts has been developed greatly, most of them focused on the modification research of the A site or the B site. There are few studies about four-way purification of PM, NO_x, CO, and HC emitted from diesel exhaust by modifying perovskite-type catalysts. A large number of studies about perovskite-type catalysts showed that the doping of the A site can help to increase the activity of the catalyst lattice oxygen and make the B site ions exist in multiple valence states, causing the increases of oxygen vacancy in the catalyst, which reduced the ignition temperature of the oxidation reaction. The A site of perovskite-type $LaCoO_3$ is the ideal adsorption site for NO_x storage. which can be doped by alkali metals, alkaline earth metals or rare earth elements. while the doping of the B site directly affects the activity of the perovskite-type catalyst, which is the redox site of the purification process, it can

be doped by transition metal elements [15,16]. The doped A or B site with other cations can rationally tune the physicochemical characteristics of perovskites, including redox performance, oxygen mobility, and ionic conductivity [17]. A large number of studies showed that the catalytic activity of perovskite was comparable to that of noble metal catalysts [18,19]. Therefore, new non-precious metal-doped perovskite-type catalysts can be developed.

In this paper, the A site of the perovskite-type $LaCoO_3$ is doped with cerium and calcium ions, and the B site is doped with iron and manganese ions. The objective of this work was to evaluate the effect of A site (cerium and calcium ions) and B site (iron and manganese ions) substitution on the structural and purification properties of perovskite-type catalyst samples. The CO, HC, and PM emitted by diesel engines are utilized as NO_x reducing agents to achieve the purpose of purifying CO, HC, NO_x, and PM simultaneously. Perovskite-type catalyst samples particles $La_{1-x}M_xCo_{1-y}N_yO_3$ with different doping amount were prepared by the sol-gel method [20,21], the prepared catalyst samples were characterized by means of XRD, FT-IR, SEM, BET, and XPS analysis. Meanwhile, by related simulation experiments and H_2 temperature-programmed reduction (H_2-TPR) experiments, the influence factors of the four-way purification efficiency were analyzed from the perspective of purification mechanism.

2. Materials and Methods

2.1. Sample Preparation

Perovskite-type catalyst samples with formula of $La_{1-x}M_xCo_{1-y}N_yO_3$ (M = Ce, Ca; N = Fe, Mn; x = 0, 0.1, 0.2, 0.3, 0.4, 0.5, 0.6; y = 0, 0.1, 0.2, 0.3, 0.4, 0.5, 0.6) were prepared by sol-gel method. $La(NO_3)_3{\cdot}6H_2O$, $Co(NO_3)_2{\cdot}6H_2O$, $Ce(NO_3)_3{\cdot}6H_2O$, $Ca(NO_3)_2{\cdot}6H_2O$, $Mn(NO_3)_2{\cdot}4H_2O$, $Fe(NO_3)_3{\cdot}9H_2O$, citrate acid, and deionized water were purchased from Shanghai Aladdin Biochemical Technology Co., Ltd., Shanghai, China. All the chemicals are analytical grade. Suitable amounts of chemicals based on stoichiometry were dissolved in deionized water to get a sol and the obtained solution was stirred vigorously using magnetic stirrer (JXX1-85-2, stirring speed 100–2000 r/min, Changzhou, China). The solution was heated on a water-bath pot (HH-1, control temperature 25–100 °C, accuracy ± 1.5 °C, Tsingtao, China); when the temperature of the solution was raised to 70 °C, a suitable amount of citric acid (the molar ratio of citric acid to metal ions is 1.2–1.5) was added and temperature was justified at 80 °C to evaporate to dryness with vigorous stirring. During the dehydration process, a poly condensation reaction carried out between nitrate ions and citric acid leading to formation of gel, the obtained wet gel was placed in a constant temperature drying box (WGL-125B, control temperature 25–300 °C, Tianjin, China) at 110 °C for 10 h to form a fluffy solid. The obtained bulk solid was placed in a Tube furnace (TL1200 Mini, Rated temperature 1100 °C, Guangzhou, China) calcined at 700 °C for 5 h and was cooled slowly to room temperature. Finally, the powders were finely ground to obtain the $La_{1-x}M_xN_yCo_{1-y}O_3$ perovskite-type catalyst samples. The preparation process route of the catalyst samples is shown in Figure 1.

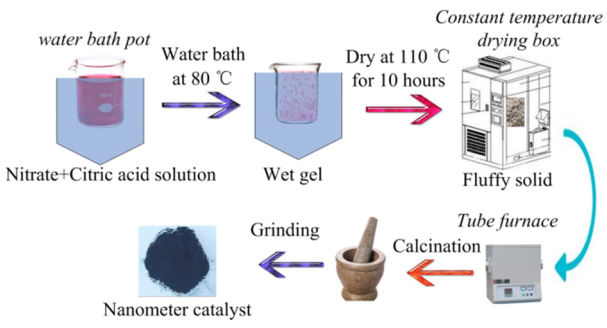

Figure 1. Preparation process route of the catalyst samples.

2.2. Characterization

The phase structure state, and ionic valence state of the catalyst crystal have a significant impact on the catalytic performance of the catalyst samples [22,23]. The phase composition of catalyst samples was characterized by an X-ray diffractometer (XRD; XRD-6100; Shimadzu, Japan) with monochromator in the continuous mode in the range 2θ = 20~80°, using Cu Kα radiation, with a scanning rate of $8° \cdot min^{-1}$ and time per step of 0.5 s. The fourier transform infrared spectrometer (FTIR; Spectrum 400; PerkinElmer, Waltham, MA, USA) as utilized to characterize the chemical composition of catalyst samples, using diffuse reflection method to test the samples that were prepared by mixing crushed catalyst samples and KBr with a mass ratio about 1:100. The number of scans was 80 and the resolution was set to 4 cm^{-1}. The Scanning Electron Microscope (SEM; Quanta 200; FEI, Valley City, ND, USA) utilized to characterize the microscopic morphology of catalyst samples. The samples were mounted on the aluminum holder with conductive adhesive and then sputtered with gold. Then the microscopic morphology of the samples was observed under the acceleration voltage of 13 kV. The N_2 adsorption isotherms and pore size distribution (PSD) curves of perovskite-type catalyst samples were measured by Automatic Surface Area and Porosity Analyzer (ASAP 2020). XPS analysis was performed on an Amicus spectrometer equipped with Mg Kα X-ray radiation.

2.3. Experimental System and Methods

A simulation test bench for activity tests of catalyst samples is shown in Figure 2. The simulated exhaust gas can be provided by the gas cylinder group 2 (O_2, N_2, C_2H_4, CO, and NO) and mixed by the gas mixing chamber 14. The tube furnace 10 was used to control the temperature of the mixed gas and the water-bath pot 6 can maintain the exhaust temperature in the Quartz tube 7. According to reference [24], the exhaust gas temperature of diesel engine is allowed to vary from 550 °C to 650 °C. Therefore, the simulated exhaust gas temperature can be maintained at 600 °C by adjusting the tube furnace. The cordierite was used to support PM and catalyst samples, the mass of supported PM and catalyst samples was 18 mg, the mass ratio of PM to catalyst samples was 1:1, the supporting process of PM and catalyst samples is shown in Figure 3. The moderate PM and catalyst samples were set in the circulating blower, which was sealed before the supporting process. When the circulating blower started, the porous structure of cordierite can capture all of the powder PM and catalyst samples. The cordierite supported with PM and catalyst samples was placed inside the quartz tube 7, the length of quartz tube is 200 mm, which is twice that of cordierite, and their diameter is 80 mm, the gas analyzer (Horida Ltd., MEXA-4000FT, relative error 1.7%, Kyoto, Japan) was used to detect the concentration of gas generated after purification, the electronic balance (PWN224ZH, repeatability deviation 0.01 mg, Shanghai, China) was used to measure the mass of cordierite before and after purification.

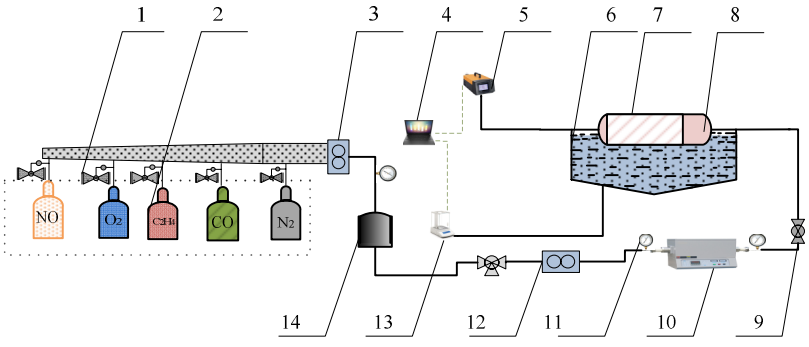

Figure 2. The overall structure of the simulation test bench. 1. Pressure-reducing valve. 2. Gas cylinder group. 3,12. Flowmeter. 4. Computer. 5. Gas analyzer. 6. Water bath pot. 7. Quartz tube. 8. Cordierite loaded with PM and catalytic agent. 9. Ball valve. 10. Tube furnace. 11. Pressure gauge. 13. Electronic balance. 14. Gas mixing chamber.

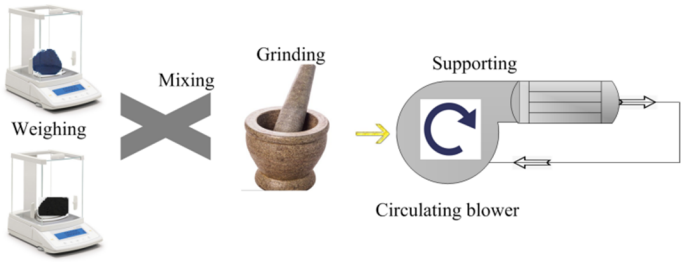

Figure 3. The supporting process of PM and catalyst samples.

All the experiments were carried out under the condition of room temperature and shading. The simulated gas was prepared by mixing O_2, N_2, C_2H_4, CO. and NO, and the gas ratio concentration was strictly controlled by the throttle valve and the flowmeter (DMF-1-S6, accuracy ± 1%), the gas flow rate of O_2, N_2, C_2H_4, CO, and NO can be controlled to 10 mL/min, 89.81 mL/min, 0.3 mL/min, 0.8 mL/min, and 0.8 mL/min separately. And the total flow rate was set to 10 mL/min, the concentration of simulated exhaust gas was shown in Table 1 [25,26]. The space velocity was 8.5×10^4 h^{-1}. When the experiment starts, the simulation test bench works stably for 10 min, according to the experimental requirements firstly. Then, experimental results were recorded and the test flow chart is shown in Figure 4. The conversion of CO, HC, NO_x, and PM were calculated as follows:

$$\eta_{CO} = \frac{C^{in}{}_{CO} - C^{out}{}_{CO}}{C^{in}{}_{CO}} \quad (1)$$

$$\eta_{HC} = \frac{C^{in}{}_{HC} - C^{out}{}_{HC}}{C^{in}{}_{HC}} \quad (2)$$

$$\eta_{NO_x} = \frac{C^{in}{}_{NO_x} - C^{out}{}_{NO_x}}{C^{in}{}_{NO_x}} \quad (3)$$

$$\eta_{PM} = \frac{M^{B}{}_{PM} - M^{A}{}_{PM}}{M^{B}{}_{PM}} \quad (4)$$

where η_{CO} is the purification efficiency of CO; $C^{in}{}_{CO}$ and $C^{out}{}_{CO}$ are concentration of before and after the experiment, ppm; η_{HC} is the purification efficiency of HC; $C^{in}{}_{HC}$ and $C^{out}{}_{HC}$ are concentration of before and after the experiment, ppm; η_{NO_x} is the purification efficiency of NO_x; $C^{in}{}_{NO_x}$ and $C^{out}{}_{NO_x}$ are concentration of before and after the experiment, ppm; η_{PM} is the purification efficiency of PM; $M^{B}{}_{PM}$ and $M^{A}{}_{PM}$ are the mass of the filter before and after the experiment, mg.

Table 1. Concentration of simulated exhaust gas pollutants.

Gas Composition	Concentration
O_2	10%
C_2H_4	300 ppm
CO	800 ppm
NO	800 ppm
N_2	dilution gas

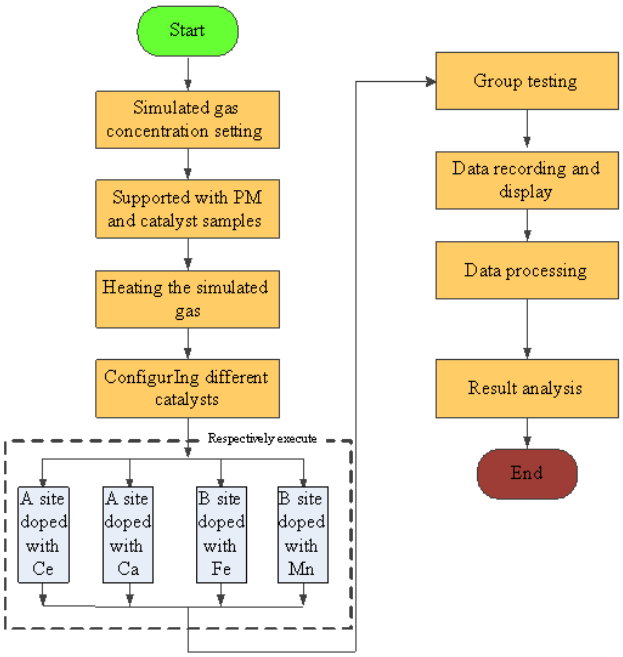

Figure 4. Simulation test flow chart.

3. Results and Discussion

3.1. Results of Characterization on Catalyst Samples Doping at A Site

X-ray diffraction patterns of catalyst samples $La_{1-x}M_xCoO_3$ (M = Ce, Ca; x = 0, 0.1, 0.2, 0.3, 0.4, 0.5, 0.6) are shown in Figure 5. As can be observed from Figure 5a, perovskite diffraction patterns were observed for $LaCoO_3$, $La_{0.9}Ce_{0.1}CoO_3$, $La_{0.8}Ce_{0.2}CoO_3$, and $La_{0.7}Ce_{0.3}CoO_3$. These samples have characteristic diffraction peaks of $LaCoO_3$ near 2θ = 23.3°, 33.0°, 42.4°, and 47.0°, and they all correspond to the perovskite-type cubic crystallized (PDF# 97-002-8921). There are CeO_2 (PDF# 97-002-8709), Co_3O_4 (PDF# 00-009-0418) impurity phases in the samples. Therefore, when Ce-content > 0.3, the XRD characteristic diffraction peaks of $LaCoO_3$ near 2θ = 33.0° was extraordinarily inconspicuous. According to reference [27], the effective ionic radius of lanthanum ions and cerium ions are 1.10 Å and 0.87 Å, respectively, therefore, excessive cerium ions and cobalt ions cannot be completely dissolved in the $LaCoO_3$ lattice. As can be observed from Figure 5b, perovskite diffraction patterns were observed for $La_{0.9}Ca_{0.1}CoO_3$, $La_{0.8}Ca_{0.2}CoO_3$, $La_{0.7}Ca_{0.3}CoO_3$, $La_{0.6}Ca_{0.4}CoO_3$, $La_{0.5}Ca_{0.5}CoO_3$, and $La_{0.4}Ca_{0.6}CoO_3$. All samples have characteristic diffraction peaks of $LaCoO_3$, and they all correspond to the perovskite-type cubic crystallized (PDF# 97-002-8921). The effective ionic radius of calcium ions is 1.06 Å, which is close to the ion radius of lanthanum ions, therefore, there are only small amounts of $CaCO_3$ (PDF# 97-002-8827) and Co_3O_4 (PDF# 00-009-0418) in the impurity phase in the crystal samples. Through the above analysis, it can be concluded that the structure of $La_{0.8}Ce_{0.2}CoO_3$ and $La_{0.8}Ca_{0.2}CoO_3$ perovskite-type catalyst samples reaches the best catalyst conditions. As can be observed from Figure 5a,b, the characteristic diffraction peaks of $LaCoO_3$ doping with cerium ions and calcium ions near 2θ = 23.3° moved left slightly. This information would confirm the accommodation of these compounds within the perovskite lattice.

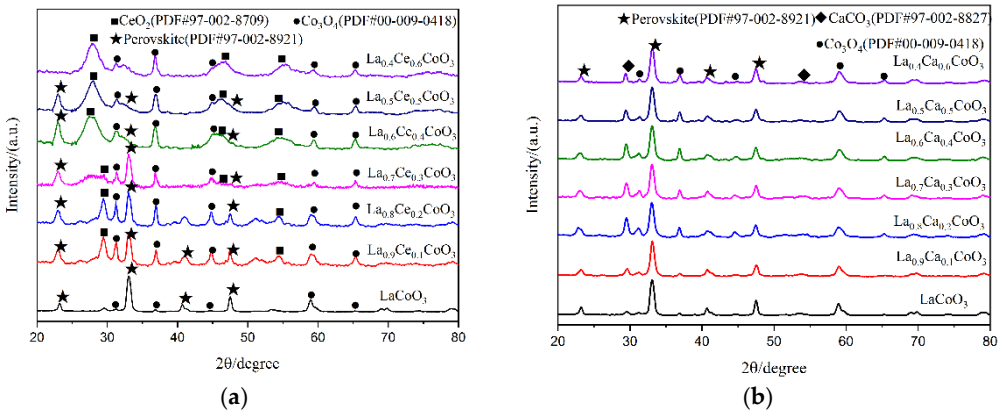

(**a**) (**b**)

Figure 5. XRD patterns of catalyst samples: (**a**) $La_{1-x}Ce_xCoO_3$ catalyst samples; and (**b**) $La_{1-x}Ca_xCoO_3$ catalyst samples.

Figure 6 shows the FT-IR spectra of $La_{0.8}Ce_{0.2}CoO_3$ and $La_{0.8}Ca_{0.2}CoO_3$ catalyst samples. As can be observed from Figure 6, there are several vibration bands at 424, 500, 596, 668, 712, 875, 1415, 1460, and 1628 cm^{-1}. FT-IR peaks located below 1000 cm^{-1} has been reported to represent metal oxides [28]. The vibration band at 424 cm^{-1} and 596 cm^{-1} belongs to the bending vibration of Co–O bonding in the BO6 octahedron, and the vibration band at 500 and 669 cm^{-1} belongs to the bending vibration of Co–O and Ce–O bonding, which are attributed to Co_3O_4 and CeO_2 [29,30]. The absorption peaks of 875 and 712 cm^{-1} belong to the calcite crystals, which are related to the bending vibration of C–O bond. The absorption peaks appeared at 1415, 1460, and 1628 cm^{-1} of catalyst samples, representing the bending mode of C–H. Compared to FTIR spectra of $La_{0.8}Ca_{0.2}CoO_3$ and $La_{0.8}Ce_{0.2}CoO_3$ catalyst samples, in the FTIR spectra of $La_{0.8}Ce_{0.2}CoO_3$, the band at 596 cm^{-1} becomes broad and up-shifting, suggesting that some amounts of Co^{3+} changed to Co^{2+} when some La^{3+} was replaced by Ce^{3+} and Ce^{4+}. However, there is no change in the valence state of Ca^{2+}, so there is no other absorption spectrum in the FTIR spectra of $La_{0.8}Ca_{0.2}CoO_3$. After the FTIR analysis, it can be confirmed that some impurities like carbonate group and hydroxyl group presented in samples.

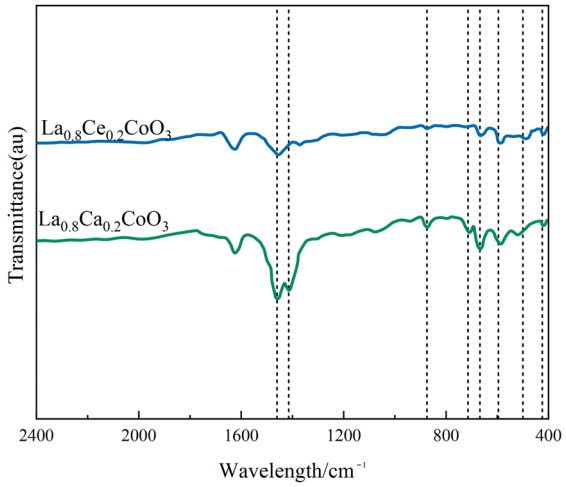

Figure 6. FTIR spectra of $La_{0.8}Ce_{0.2}CoO_3$ and $La_{0.8}Ca_{0.2}CoO_3$ catalyst samples.

3.2. Results of Simulation Experiments on Catalyst Samples Doping at A Site

MATLAB software was used to fit the experimental data. Figure 7a–d show the time curve of the purification efficiency of NO_x, PM, HC, and CO when the A site was doped with different concentrations of cerium ions. As can be observed from Figure 7, when the purification time does not exceed 90 s, the purification efficiency increases with time. At

this time, the catalyst samples are in the heating stage and do not exert the best catalytic performance. When the time exceeds 90 s, the purification efficiency reaches the highest. When the purification time exceeds 120 s, the purification efficiencies of NO_x and PM show an obvious downward trend, which can be attributed to the decrease of PM load with purification time increases, decreasing the NO_x and PM redox reaction rate. When the doping amount does not exceed 0.2, the purification efficiencies of NO_x, PM, HC, and CO improve with the increase of the doping amount. When x = 0.2, the purification efficiency can reach the highest, which can reach 85%, 90%, 94%, and 100%, respectively. When x > 0.3, excessive cerium ions were not doped in perovskite-type oxide, too much impurity phase was introduced into the catalyst samples. These impurities have poor purification efficiency on NO_x, PM, HC, and CO, which are consistent with the results of XRD.

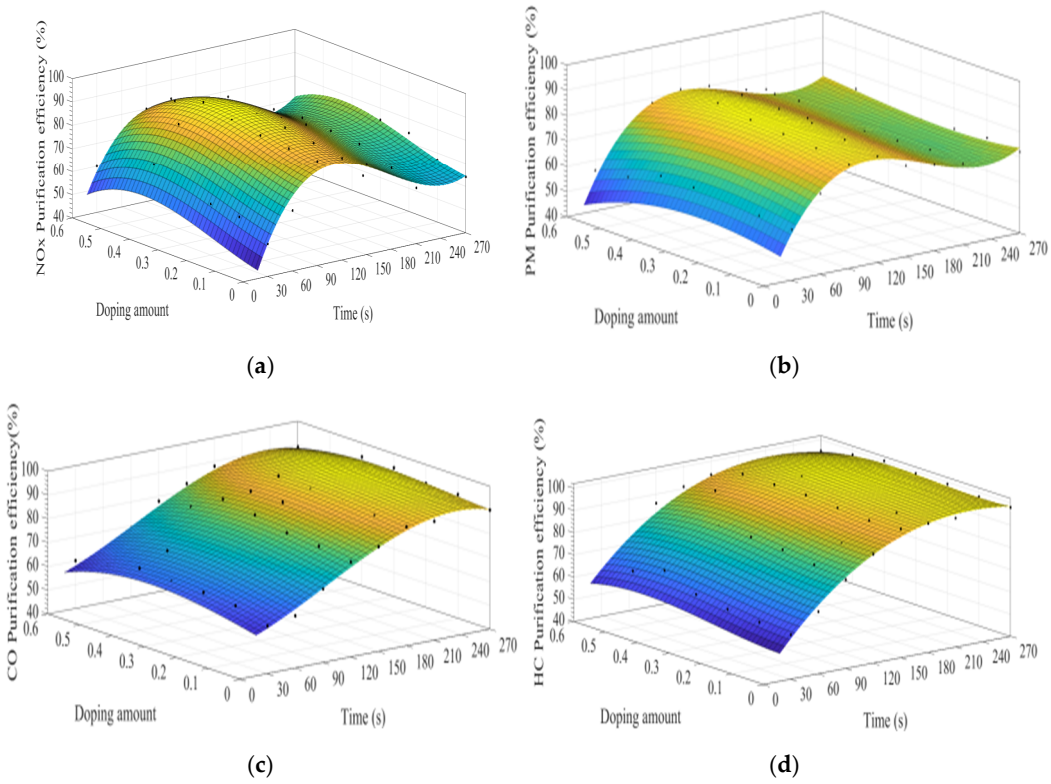

Figure 7. Purification efficiency curve of catalyst when A site was doped with ceriumions: (**a**) NO_x; (**b**) PM; (**c**) CO; and (**d**) HC.

Figure 8a–d show the time curve of the purification efficiency of NO_x, PM, HC, and CO when the A site was doped with different concentrations of calcium ions. Upon comparison of perovskite-type catalyst samples doped with calcium ions and cerium ions, the purification trend and efficiency of PM, HC, and CO are basically the same. However, the doping of calcium ions shows a lower efficiency in purifying NO_x, and the highest purification efficiency is 72%, which can be attributed to the factor that the valence state of the doped calcium ions has not changed, and the Co^{3+} in the catalyst samples change to Co^{4+}, but not to Co^{2+}. The existence of Co^{2+} is more conducive to the formation of O vacancies and adsorbed NO, which is beneficial to the reduction of NO, and the change of ions valence state promotes the adsorption and desorption of O. In addition, When A-site of $LaCoO_3$ perovskite was doped with cerium ions, the catalyst crystal produces small distortion and enhances the purification efficiency of PM, NO_x, CO, and HC, which is consistent with the research content reported in the literature [3–31]. According to the literature [32–36] on the mechanism analysis of purifying the exhaust pollutants by

perovskite-type catalysts, combined with the experiment results of this study, the overall purification and purification process is inferred as Formulas (5)–(19).

$$NO \leftrightarrow NO_{ads} \quad (5)$$

$$CO \leftrightarrow CO_{ads} \quad (6)$$

$$2N_{ads} \leftrightarrow N_2 \quad (7)$$

$$O_2 \leftrightarrow 2O_{ads} \quad (8)$$

$$C_2H_4 \leftrightarrow C_2H_{3ads} + H_{ads} \quad (9)$$

$$NO_{ads} \rightarrow N_{ads} + O_{ads} \quad (10)$$

$$CO_{ads} + O_{ads} \rightarrow CO_2 \quad (11)$$

$$PM + O_{ads} \rightarrow CO_2 + CO \quad (12)$$

$$NO_{ads} + O_{ads} \rightarrow NO_2 \quad (13)$$

$$PM + NO_{2ads} \rightarrow CO + CO_2 + N_2 \quad (14)$$

$$CO_{ads} + NO_{2ads} \rightarrow CO_2 + N_2 \quad (15)$$

$$C_2H_{3ads} + NO_{2ads} \rightarrow CO_2 + N_2 + H_2O \quad (16)$$

$$H_{ads} + NO_{2ads} \rightarrow N_2 + H_2O \quad (17)$$

$$H_{ads} + NO_{ads} \rightarrow N_2 + H_2O \quad (18)$$

$$C_2H_{3ads} + NO_{ads} \rightarrow CO_2 + N_2 + H_2O \quad (19)$$

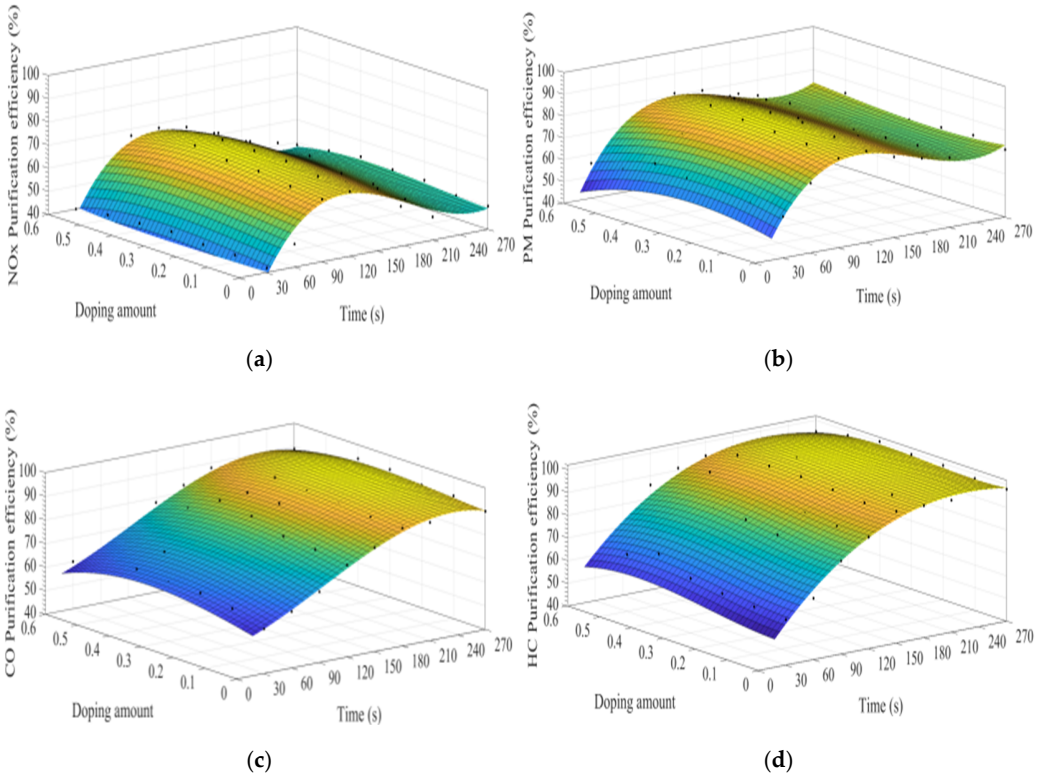

Figure 8. Purification efficiency curve of catalyst when A site was doped with calcium ions: (**a**) NO_x; (**b**) PM; (**c**) CO; and (**d**) HC.

The deconvolution of O 1 s signals was conducted in order to estimate the species in detail. As shown in Figure 9, The O 1 s spectrum for $La_{0.8}Ca_{0.2}CoO_3$ and $La_{0.8}Ce_{0.2}CoO_3$ could be decomposed into two components. The peak at about 529.1 eV was ascribed to the lattice oxygen species (O_{latt}). Another component at 531.2 eV was assigned to adsorbed oxygen species (O_{ads}) [37], which has been reported as active species in oxidation reactions due to the electrophilic nature [38]. Since the surface O_{ads}/O_{latt} molar ratio of the $La_{0.8}Ce_{0.2}CoO_3$ sample (0.78) was higher than that of the $La_{0.8}Ca_{0.2}CoO_3$ sample (0.62). Therefore, the $La_{0.8}Ce_{0.2}CoO_3$ sample showed the better purification efficiency in NO, which are consistent with the reaction pathway reported in Equations (5)–(19).

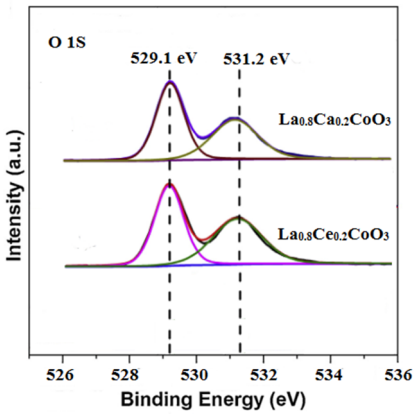

Figure 9. X-ray photoelectron of the O 1 s for $La_{0.8}Ca_{0.2}CoO_3$ and $La_{0.8}Ce_{0.2}CoO_3$.

The SEM micrographs clearly show large differences in the micro-structure and morphology of $La_{0.8}Ce_{0.2}CoO_3$ and $La_{0.8}Ca_{0.2}CoO_3$ perovskite-type catalyst samples from Figure 10a,b, $La_{0.8}Ce_{0.2}CoO_3$ perovskite-type catalyst samples represent porous morphologies, $La_{0.8}Ca_{0.2}CoO_3$ perovskite-type catalyst samples represent spongy morphologies. Both samples are uniformly dispersed without sintering. The porous structure of $La_{0.8}Ce_{0.2}CoO_3$ perovskite-type catalyst samples are clearer than $La_{0.8}Ca_{0.2}CoO_3$, the pore size of which ranging from 3 μm to 5 μm.

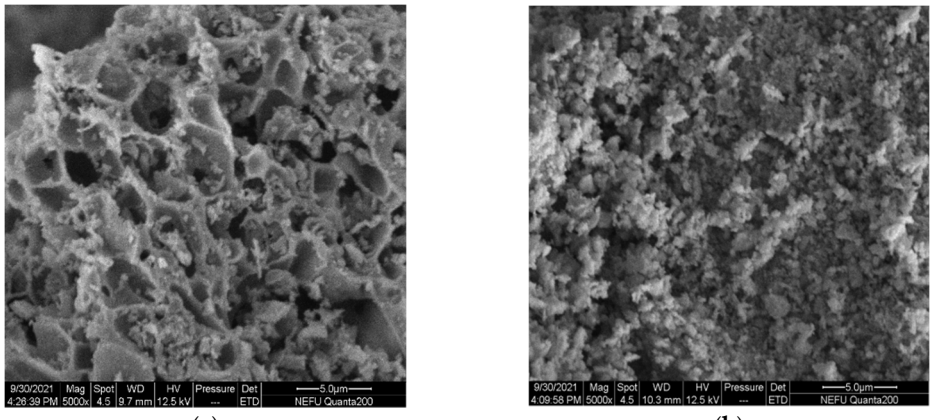

(**a**) (**b**)

Figure 10. SEM of catalyst samples: (**a**) $La_{0.8}Ce_{0.2}CoO_3$; and (**b**) $La_{0.8}Ca_{0.2}CoO_3$.

3.3. Results of Characterization on Catalyst Samples Doping at B Site

On the basis of the above research results, the A-site doping amount of cerium ions was selected, and the doping amount was 0.2. The B-site doping of manganese and iron ions on the catalytic performance of the La-based perovskite-type catalyst should be further studied. According to reference [27], the effective ionic radius of iron ions, cobalt ions and manganese ions are 0.645 Å, 0.61 Å, and 0.645 Å, respectively, which meet the 15% rule.

Therefore, $La_{0.8}Ce_{0.2}Co_{1-y}N_yO_3$ (N = Fe, Mn; y = 0, 0.1, 0.2, 0.3, 0.4, 0.5, 0.6) can form continuous series of solid solutions.

X-ray diffraction patterns of catalyst samples $La_{0.8}Ce_{0.2}Co_{1-y}N_yO_3$ (N = Fe, Mn; y = 0, 0.1, 0.2, 0.3, 0.4, 0.5, 0.6) are shown in Figure 11. As can be observed from Figure 11a, perovskite diffraction patterns can be observed for $La_{0.8}Ce_{0.2}Co_{0.9}Fe_{0.1}O_3$, $La_{0.8}Ce_{0.2}Co_{0.8}Fe_{0.2}O_3$, $La_{0.8}Ce_{0.2}Co_{0.7}Fe_{0.3}O_3$, $La_{0.8}Ce_{0.2}Co_{0.6}Fe_{0.4}O_3$, $La_{0.8}Ce_{0.2}Co_{0.5}Fe_{0.5}O_3$, and $La_{0.8}Ce_{0.2}Co_{0.4}Fe_{0.6}O_3$. All samples have characteristic diffraction peaks of $LaCoO_3$ near 2θ = 23.3°, 33.0°, 42.4°, and 47.0°, they all correspond to the perovskite-type cubic crystallized (PDF# 97-002-8921). There are CeO_2 (PDF# 97-002-8709), FeO (PDF# 97-008-2236), and Fe_3O_4 (PDF# 00-026-1136), as well as a small amount of Co_3O_4 (PDF# 00-009-0418) impurity phases in the crystal samples. However, the doping of iron ions enhances the solubility of cerium ions in the crystal lattice. As can be observed from Figure 11b, perovskite diffraction patterns can be observed for $La_{0.8}Ce_{0.2}Co_{0.9}Mn_{0.1}O_3$, $La_{0.8}Ce_{0.2}Co_{0.8}Mn_{0.2}O_3$, $La_{0.8}Ce_{0.2}Co_{0.7}Mn_{0.3}O_3$, and $La_{0.8}Ce_{0.2}Co_{0.6}Mn_{0.4}O_3$, they all correspond to the perovskite-type cubic crystallized. There are amount of MnO_2 (PDF# 00-053-0633), CeO_2 (PDF# 97-002-8709), and Co_3O_4 (PDF# 00-009-0418) impurity phases in the crystal samples. $LaCoO_3$ perovskite seems to accept a higher cobalt ions substitution degree by iron ions than manganese ions, without destabilizing the perovskite structure. In fact, the continuous series of solid solutions of atoms in perovskite crystals has not been realized. This may be due to the fact that cerium atoms cannot achieve continuous series of solid solutions in perovskite crystals. Through the above analysis, it can be concluded that the structure of $La_{0.8}Ce_{0.2}Co_{0.7}Fe_{0.3}O_3$ and $La_{0.8}Ce_{0.2}Co_{0.7}Mn_{0.3}O_3$ perovskite-type catalyst samples reaches the best catalyst conditions. As can be observed from Figure 11a,b, the characteristic diffraction peaks of $La_{0.8}Ce_{0.2}CoO_3$ doping with cerium ions and calcium ions near 2θ = 33° moved right slightly. This information would confirm the accommodation of these compounds within the perovskite lattice.

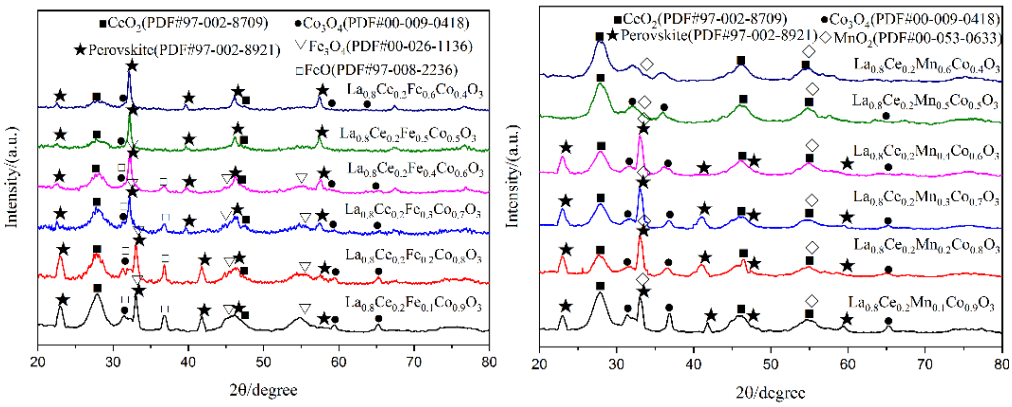

(**a**) (**b**)

Figure 11. XRD patterns of catalyst samples: (**a**) $La_{0.8}Ce_{0.2}Co_{1-y}Fe_yO_3$ catalyst samples; and (**b**) $La_{0.8}Ce_{0.2}Co_{1-y}Mn_yO_3$ catalyst samples.

Figure 12 shows the FT-IR spectra of $La_{0.8}Ce_{0.2}Co_{0.7}Fe_{0.3}O_3$ and $La_{0.8}Ce_{0.2}Co_{0.7}Mn_{0.3}O_3$ catalyst samples. As can be observed from Figure 12, there are several vibration bands at 424, 470, 500, 530, 543, 550, 561, 562, 596, 668, 1460, and 1628 cm^{-1} for $La_{0.8}Ce_{0.2}Co_{0.7}Fe_{0.3}O_3$ and $La_{0.8}Ce_{0.2}Co_{0.7}Mn_{0.3}O_3$ catalyst samples. The vibration band at 470 and 550 cm^{-1} belongs to the bending vibration of Fe–O bonding in the BO_6 octahedron, and the peak at 561 cm^{-1} is attributed to asymmetrical modes of the Mn–O bond of MnO_6 octahedrons groups of $LaMnO_3$ perovskite. The vibration band at 543 and 560 cm^{-1} belongs to the bending vibration of Fe–O bonding in the FeO and Fe_3O_4 crystals, respectively. The vibration band at 530 cm^{-1} belongs to the bending vibration of Mn–O bonding in the MnO_2 crystals [39,40]. Several vibration band of some impurities like carbonate group and hydroxyl group also can be observed from Figure 12, which would not be analysed in this paper.

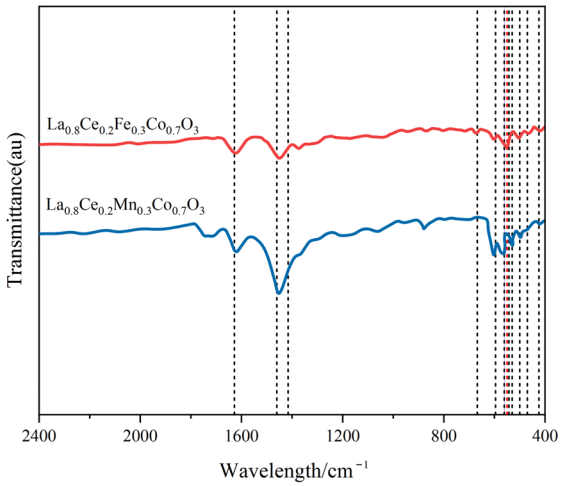

Figure 12. FTIR spectra of $La_{0.8}Ce_{0.2}Fe_{0.3}Co_{0.7}O_3$ and $La_{0.8}Ce_{0.2}Mn_{0.3}Co_{0.7}O_3$ catalyst samples.

3.4. Results of Simulation Experiments on Catalyst Samples Doping at B Site

Figure 13a–d shows the fitting curves of the purification efficiencies of NO_x, PM, HC, and CO over time when the B site was doped with different concentrations of iron ions. As can be observed from Figure 13, when the purification time does not exceed 90 s, the purification efficiency increases with time. When the time exceeds 90 s, the purification efficiency reaches the highest. When the purification time exceeds 180 s, the purification efficiency of NO_x and PM shows an obvious downward trend. When y = 0.3, the purification efficiency can reach the highest. Compared with $La_{0.8}Ce_{0.2}CoO_3$, the highest purification efficiency for PM and NO_x is increased by 5% and 7%, respectively, while the purification efficiency for HC and CO is hardly improved.

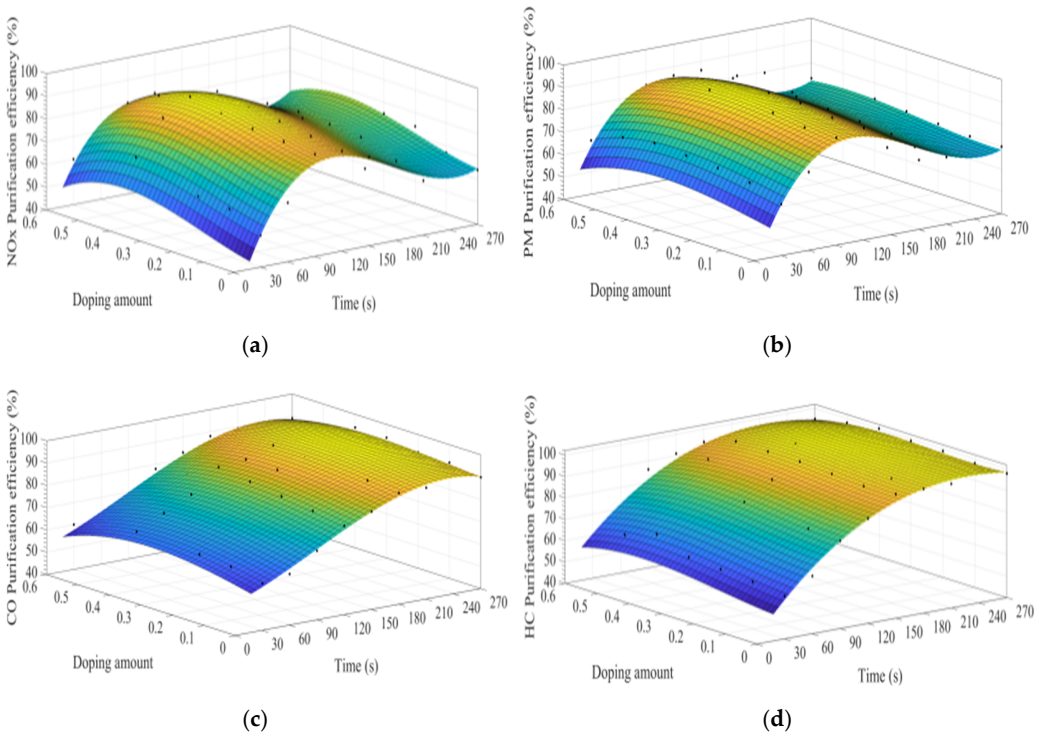

Figure 13. Purification efficiency curve of catalyst when B site was doped with iron ions: (**a**) NO_x; (**b**) PM; (**c**) CO; and (**d**) HC.

Figure 14a–d shows the time curve of the purification efficiency of NO_x, PM, HC, and CO when the B site is doped with different concentrations of manganese ions. Comparison of perovskite-type catalysts doped with iron ions and manganese ions, the purification trend of NO_x, PM, HC, and CO are basically the same. Compared with $La_{0.8}Ce_{0.2}CoO_3$, when y = 0.3, the highest purification efficiency for PM and NO_x is increased by 6% and 2%, which can be speculated that the doping of manganese ions at the B site is more conducive to the oxidation reaction, and the doping of iron ions at the B site is more conducive to the reduction reaction.

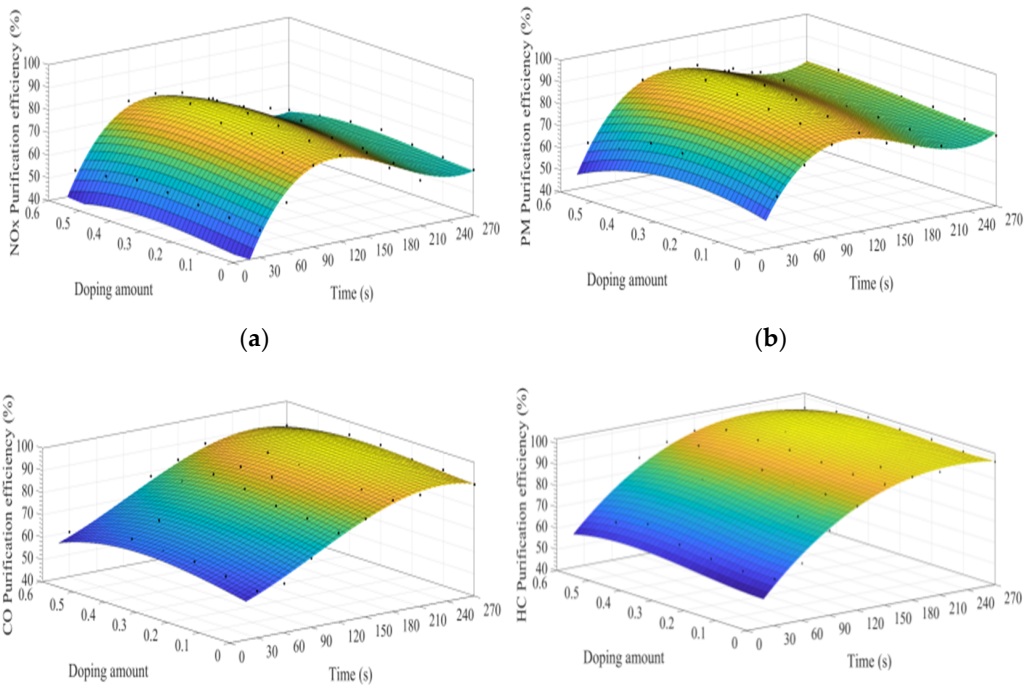

Figure 14. Purification efficiency curve of catalyst when B site was doped with manganese ions: (**a**) NO_x; (**b**) PM; (**c**) CO; and (**d**) HC.

The H_2-TPR experiments were conducted on a TPDRO instrument (TP-5080, Xianquan, Tianjin, China) using a thermal conductivity detector (TCD). H_2-TPR techniques were used to measure the reducibility of $La_{0.8}Ce_{0.2}Co_{0.7}Fe_{0.3}O_3$ and $La_{0.8}Ce_{0.2}Co_{0.7}Mn_{0.3}O_3$ catalyst samples. The corresponding H_2-TPR profiles are presented in Figure 15. Both of the samples exhibit two major reduction peaks, the first reduction peak of $La_{0.8}Ce_{0.2}Co_{0.7}Fe_{0.3}O_3$ at 340 °C can be attributed to the reduction of Fe^{4+} to Fe^{3+} and consumption of adsorbed oxygen [41]. The first reduction peak of $La_{0.8}Ce_{0.2}Co_{0.7}Mn_{0.3}O_3$ at 339 °C can be attributed to the reduction of Mn^{4+} to Mn^{3+} consumption of adsorbed oxygen [42]. The second reduction peak of $La_{0.8}Ce_{0.2}Co_{0.7}Fe_{0.3}O_3$ appears at 551 °C, which can be ascribed to the reduction of Fe^{3+} to Fe^{2+} and consumption of lattice oxygen [43]. The second reduction peak of $La_{0.8}Ce_{0.2}Co_{0.7}Mn_{0.3}O_3$ appears at 762 °C, which can be ascribed to the reduction of Mn^{3+} to Mn^{2+} and consumption of lattice oxygen [44]. Through the analysis above, it can be concluded that the redox properties and the oxygen mobility of the catalysts are important influencing factors in purification efficiency of NO_x, PM, HC, and CO.

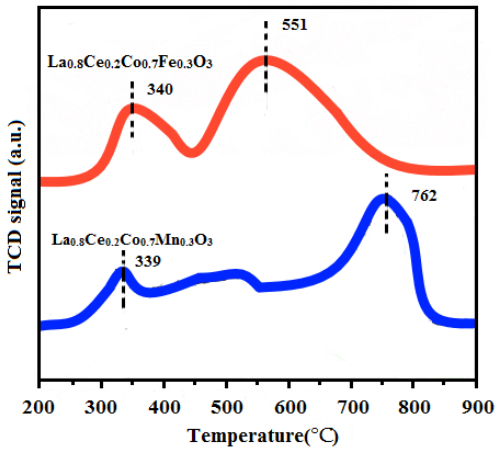

Figure 15. H_2-TPR profiles of $La_{0.8}Ce_{0.2}Co_{0.7}Fe_{0.3}O_3$ and $La_{0.8}Ce_{0.2}Co_{0.7}Mn_{0.3}O_3$.

The SEM micrographs of $La_{0.8}Ce_{0.2}Co_{0.7}Fe_{0.3}O_3$ and $La_{0.8}Ce_{0.2}Co_{0.7}Mn_{0.3}O_3$ perovskite-type catalyst crystal samples are shown in Figure 16a,b, $La_{0.8}Ce_{0.2}Co_{0.7}Fe_{0.3}O_3$ perovskite-type catalyst samples are more uniformly dispersed, and $La_{0.8}Ce_{0.2}Co_{0.7}Mn_{0.3}O_3$ perovskite-type catalyst samples are partially reunited. Both of the perovskite-type catalyst samples exist porous structure. The macropore with diameter ranging from 3 μm to 5 μm in perovskite-type catalyst samples. Perovskite-type catalyst crystal samples can contact the PM and hazardous gas sufficiently emitted from engine owing to their high specific surface area and porosity [45]. $La_{0.8}Ce_{0.2}Co_{0.7}Fe_{0.3}O_3$ perovskite-type catalyst samples were more conducive to the application in the field of automobile exhaust purification.

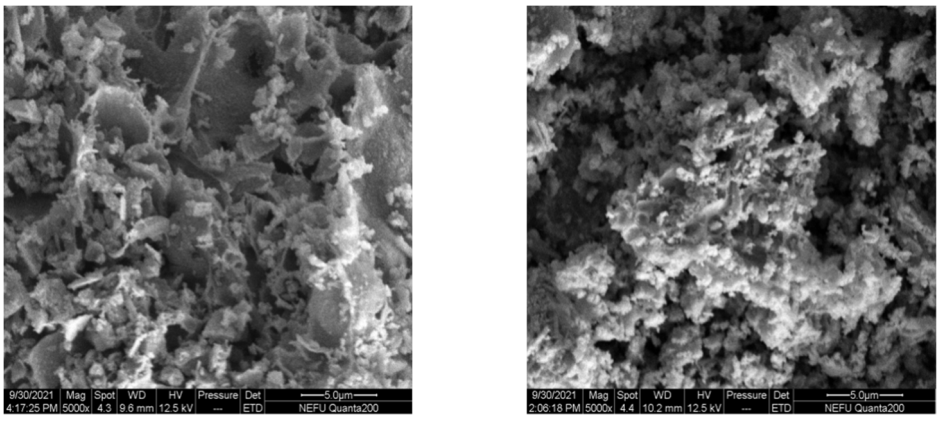

(**a**) (**b**)

Figure 16. SEM of catalyst samples: (**a**) $La_{0.8}Ce_{0.2}Co_{0.7}Fe_{0.3}O_3$; and (**b**) $La_{0.8}Ce_{0.2}Co_{0.7}Mn_{0.3}O_3$.

Figure 17a,b show N_2 adsorption isotherms and pore size distribution (PSD) curves of $LaCoO_3$, $La_{0.8}Ce_{0.2}Fe_{0.3}Co_{0.7}O_3$, and $La_{0.8}Ce_{0.2}Co_{0.7}Mn_{0.3}O_3$ perovskite-type catalyst samples separately. Based on the International Union of Pure and Applied Chemistry classification (IUPAC), the isotherms curves in Figure 17a reveals an H3 hysteresis loop related to mesoporous or macroporous materials. It can be seen that the order of specific surface area is $LaCoO_3$, $La_{0.8}Ce_{0.2}Fe_{0.3}Co_{0.7}O_3$, and $La_{0.8}Ce_{0.2}Co_{0.7}Mn_{0.3}O_3$. Significant increase in nitrogen adsorption at high relative pressure ($0.9 < P/P_0 < 1$) and the PSD curves illustrate the extensive existence of the mesopores and macropore, which are well consistent with the analysis of SEM. Figure 17b reveals that $La_{0.8}Ce_{0.2}Fe_{0.3}Co_{0.7}O_3$ perovskite -type catalyst sample has the largest pore volume of mesopores (mainly concentrated in 50 nm). The detailed textural parameters of catalyst samples are listed in Table 2. It is widely accepted that the impurities formation as a consequence of the limited accommodation of A and B cations leads to a progressive decrease of specific surface area [46]. Based on the above analysis, it

can be further inferred that the impurity content of $La_{0.8}Ce_{0.2}Co_{0.7}Fe_{0.3}O_3$ perovskite-type catalyst crystal samples is less than that of $La_{0.8}Ce_{0.2}Co_{0.7}Mn_{0.3}O_3$ perovskite-type catalyst crystal samples, which are consistent with the results of XRD and FT-IR.

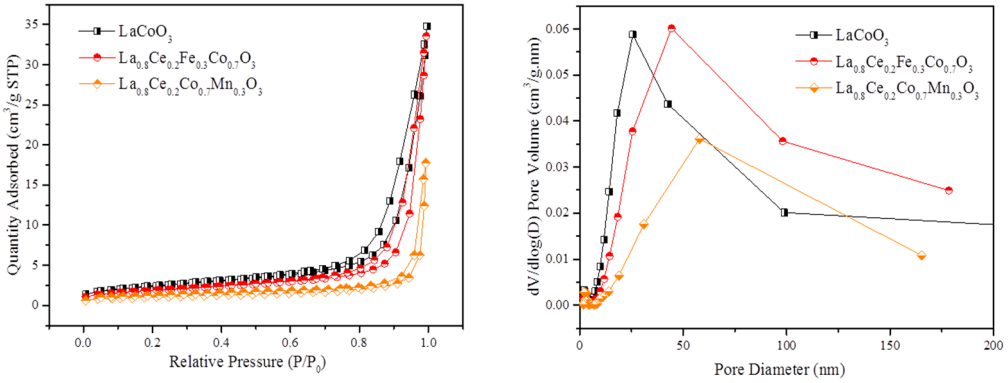

(**a**) (**b**)

Figure 17. N_2 adsorption isotherms and PSD curves of catalyst samples: (**a**) N_2 adsorption isotherms; and (**b**) PSD curves.

Table 2. The Textural parameters of catalyst samples.

Samples	BET Surface Area (m^2/g)	Average Pore Diameter (nm)
$LaCoO_3$	8.19	26.75
$La_{0.8}Ce_{0.2}Fe_{0.3}Co_{0.7}O_3$	6.38	34.50
$La_{0.8}Ce_{0.2}Co_{0.7}Mn_{0.3}O_3$	3.63	39.64

Based on the above analysis, the purification data for the best samples (x = 0.2; y = 0; 0.3) are shown in Table 3. It can be seen that appropriate doping of A and B sites is effective for the four-way purification efficiency. Combined with the analysis results of t SEM and BET, $La_{0.8}Ce_{0.2}Co_{0.7}Fe_{0.3}O_3$ perovskite-type catalyst samples can be further proved to be the optimal doping concentration.

Table 3. The purification data for the best samples (x = 0.2; y = 0; 0.3).

Purification Data (%) / Doping Amount	NO_x	PM	HC	CO
M = Ce; x = 0.2; y = 0	85	90	94	100
M = Ca; x = 0.2; y = 0	72	90	94	100
M = Ce; N = Mn; x = 0.2; y = 0.3	87	96	94	100
M = Ce; N = Fe; x = 0.2; y = 0.3	92	95	94	100

4. Conclusions

Several perovskite-type catalyst samples were developed for the four-way purification of diesel engine exhaust by doping A and B Sites in perovskite $LaCoO_3$. The prepared perovskite-type catalyst samples were characterized by XRD, SEM, FT-IR, and BET analysis, and their activity were tested by simulation experiments. The following conclusions were reached:

1. The porous perovskite structures can be observed from prepared perovskite-type catalyst samples. When the A-site and B-site doping amount of $LaCoO_3$ exceeds a certain value, more impurity phases will be produced;
2. Macropores of 3 μm to 5 μm are presented in $La_{0.8}Ce_{0.2}Fe_{0.3}Co_{0.7}O_3$ and $La_{0.8}Ce_{0.2}Co_{0.7}Mn_{0.3}O_3$ perovskite-type catalyst samples, and $La_{0.8}Ce_{0.2}Fe_{0.3}Co_{0.7}O_3$ has the largest pore volume of mesopores (mainly concentrated in 50 nm);

3. Doping the A site of $LaCoO_3$ perovskite-type oxide can change the valence state of the B site ions to a certain extent, which is conducive to the occurrence of redox reactions;
4. On the basis of cerium ions doping the A site of $LaCoO_3$ perovskite-type oxide, the doping of manganese ions at the B site can further improve the purification ability on PM. However, the doping of iron ions at the B site can enhance the purification ability on PM and NO_x; and
5. $La_{0.8}Ce_{0.2}Co_{0.7}Fe_{0.3}O_3$ shows the best purification ability and the least impurity phase in the samples, the purification efficiency of PM, NO_x, HC, and CO are 95%, 92%, 94%, and 100%, respectively.

Author Contributions: X.G. and Y.W., data curation; Y.W. and S.Y., formal analysis; D.D. and S.Y., resources; Y.W. and D.D. methodology, Y.W. writing—original draft; X.G. and Y.W., writing—review and editing; X.G., funding acquisition and supervision. All authors have read and agreed to the published version of the manuscript.

Funding: This research was supported by the National Natural Science Foundation of China (grant number 51972050).

Institutional Review Board Statement: Not applicable.

Informed Consent Statement: Not applicable.

Data Availability Statement: Data can be made available upon request.

Acknowledgments: The authors gratefully acknowledge the academic support of the Lab of Automobile Emission Testing and Control Laboratory, College of Mechanical and Electric Engineering at Northeast Forestry University, Harbin, China.

Conflicts of Interest: The authors declare that they have no known competing financial interests or personal relationships that could have influenced, or appeared to have influenced, the work reported in this paper.

References

1. Fujita, E.M.; Zielinska, B.; Campbell, D.E.; Arnott, W.P.; Sagebiel, J.C.; Mazzoleni, L.; Chow, J.C.; Gabele, P.A.; Crews, W.; Snow, R.; et al. Variations in Speciated Emissions from Spark-Ignition and Compression-Ignition Motor Vehicles in California's South Coast Air Basin. *J. Air Waste Manag. Assoc.* **2007**, *57*, 705–720. [CrossRef] [PubMed]
2. Wu, J.-Z.; Ge, D.-D.; Zhou, L.-F.; Hou, L.-Y.; Zhou, Y.; Li, Q.-Y. Effects of particulate matter on allergic respiratory diseases. *Chronic Dis. Transl. Med.* **2018**, *4*, 95–102. [CrossRef] [PubMed]
3. Cheng, Y.; Liu, J.; Zhao, Z.; Song, W.; Wei, Y. A new 3DOM Ce-Fe-Ti material for simultaneously catalytic removal of PM and NO_x from diesel engines. *J. Hazard. Mater.* **2018**, *342*, 317–325. [CrossRef] [PubMed]
4. Pacultová, K.; Draštíková, V.; Chromčcáková, Ž.; Bílková, K.T.; Kutláková, M.; Kotarba, A.; Obalová, L. On the stability of alkali metal promoters in Co mixed oxides during direct NO catalytic decomposition. *Mol. Catal.* **2017**, *428*, 33–40. [CrossRef]
5. Peña, M.A.; Fierro, J.L.G. Chemical Structures and Performance of Perovskite Oxides. *Chem. Rev.* **2001**, *101*, 1981–2018. [CrossRef]
6. Dhal, G.C.; Mohan, D.; Prasad, R. Preparation and application of effective different catalysts for simultaneous control of diesel soot and NO_x emissions: An overview. *Catal. Sci. Technol.* **2017**, *7*, 1803–1825. [CrossRef]
7. Wang, H.; Li, C.; Hu, Y.; Chi, Y.; Song, Y.; Ren, X. Research into Eliminating Particulate from Diesel Engine Exhaust over Zeolite Covered with Catalysts of Perovskite-Type Oxides. In Proceedings of the International Conference on Energy and Environment Technology, Guilin, China, 16–18 October 2009.
8. Mei, X.; Xiong, J.; Wei, Y.; Zhang, Y.; Zhang, P.; Yu, Q.; Zhao, Z.; Liu, J. High-efficient non-noble metal catalysts of 3D ordered macroporous perovskite-type La2NiB'O6 for soot combustion: Insight into the synergistic effect of binary Ni and B' sites. *Appl. Catal. B Environ.* **2020**, *275*, 119108. [CrossRef]
9. Abedi, S.; Niaei, A.; Namjou, N.; Salari, D.; Tarjomannejad, A.; Izadkhah, B. Experimental and Modeling Study of CO-Selective Catalytic Reduction of NO Over Perovskite-Type Nanocatalysts. *Period. Polytech. Chem. Eng.* **2020**, *64*, 46–53. [CrossRef]
10. Fang, F.; Zhao, P.; Feng, N.; Wan, H.; Guan, G. Surface engineering on porous perovskite-type $La_{0.6}Sr_{0.4}CoO_3$-δ nanotubes for an enhanced performance in diesel soot elimination. *J. Hazard. Mater.* **2020**, *399*, 123014. [CrossRef]
11. Jiang, Q.; Cao, Y.; Liu, X.; Zhang, H.; Hong, H.; Jin, H. Chemical Looping Combustion over a Lanthanum Nickel Perovskite-Type Oxygen Carrier with Facilitated O_2-Transport. *Energy Fuels* **2020**, *34*, 8732–8739. [CrossRef]
12. Magnone, E.; Kim, J.R.; Park, J.H. Effect of synthesis method on oxygen adsorption/desorption properties of La-Sr-Co-FeO perovskite-typeoxide. *J. Anal. Calorim.* **2014**, *117*, 1221–1229. [CrossRef]

13. Tang, L.; Zhao, Z.; Li, K.; Yu, X.; Wei, Y.; Liu, J.; Peng, Y.; Li, Y.Z.; Chen, Y.S. Highly active monolith catalysts of $LaKCoO_3$ perovskite-type complex oxide on alumina-wash coated diesel particulate filter and the catalytic performances for the combustion of soot. *Catal. Today* **2020**, *339*, 159–173. [CrossRef]
14. Zhang, S.; An, K.; Li, S.; Zhang, Z.; Sun, R.; Liu, Y. Bi-active sites of stable and highly dispersed platinum and oxygen vacancy constructed by reducing a loaded perovskite-type oxide for CO oxidation. *Appl. Surf. Sci.* **2020**, *532*, 147455. [CrossRef]
15. Peng, X.; Lin, H.; Shangguan, W.; Huang, Z. A highly efficient and porous catalyst for simultaneous removal of NO_x and diesel soot. *Catalysis Communications* **2007**, *8*, 157–161. [CrossRef]
16. De Lim, S.M.; Assaf, J.M. Synthesis and characterization of $LaNiO_3$, $LaNi_{(1-x)}Fe_xO_3$ and $LaNi_{(1-x)}Co_xO_3$ perovskite oxides for catalysis application. *Mater. Res. Bull.* **2002**, *5*, 329–335.
17. Yan, X.; Liu, J.; Yang, Y.; Wang, Z.; Zheng, Y. A catalytic reaction scheme for NO reduction by CO over Mn-terminated $LaMnO_3$ perovskite: A DFT study. *Fuel Processing Technol.* **2021**, *216*, 106798. [CrossRef]
18. Ma, Y.; Ma, Y.; Long, G.; Buckley, C.E.; Hu, X.; Dong, D. Electrospun $La_{0.8}Ce_{0.2}Fe_{1-x}Ni_xO_3$ perovskite nanofibrous catalysts for CO oxidation. *Appl. Surf. Sci. Adv.* **2020**, *2*, 100030. [CrossRef]
19. Onrubia-Calvo, J.A.; Pereda-Ayo, B.; De-La-Torre, U.; González-Velasco, J.R. Strontium doping and impregnation onto alumina improve the NO_x storage and reduction capacity of $LaCoO_3$ perovskites. *Catal. Today* **2019**, *333*, 208–218. [CrossRef]
20. Natile, M.M.; Ugel, E.; Maccato, C.; Glisenti, A. $LaCoO_3$: Effect of synthesis conditions on properties and reactivity. *Appl. Catal. B Environ.* **2007**, *72*, 351–362. [CrossRef]
21. Zhao, P.; Fang, F.; Feng, N.; Chen, C.; Liu, G.; Chen, L.; Zhu, Z.; Meng, J.; Wan, H.; Guan, G. Self-templating construction of mesopores on three-dimensionally ordered macroporous $La_{0.5}Sr_{0.5}MnO_3$ perovskite with enhanced performance for soot combustion. *Catal. Sci. Technol.* **2019**, *9*, 1835–1846. [CrossRef]
22. Xing, Z.; Kongzhai, L.; Neal, L.M.; Fanxing, L. Perovskites as geo-inspired oxygen storage materials for chemical looping and three-way catalysis—A perspective. *ACS Catal.* **2018**, *8*, 8213–8236.
23. Yu, L.; Zhong, Q.; Deng, Z.; Zhang, S. Enhanced NO_x removal performance of amorphous Ce-Ti catalyst by hydrogen pretreatment. *J. Mol. Catal. A Chem.* **2016**, *423*, 371–378. [CrossRef]
24. Kim, J.H.; Kim, M.Y.; Kim, H.G. NO_2-Assisted Soot Regeneration Behavior in a Diesel Particulate Filter with Heavy-Duty Diesel Exhaust Gases. *Numer. Heat Transf. Part A Appl.* **2010**, *58*, 725–739. [CrossRef]
25. Danfeng, D.; Yinghui, W.; Xiurong, G. Experiment on the performance of the NTP synergisticwood fiber diesel exhaust purifier. *J. Harbin. Eng. Univ.* **2019**, *40*, 419–425.
26. Qin, X.; Jie, X. *Modern Catalytic Chemistry*; Science Press: Beijing, China, 2016; pp. 310–312.
27. Shannon, R.D. Revised effective ionic radii and systematic studies of interatomic distances in halides and chalcogenides. *Acta Crystallogr. Sect. A* **1976**, *32*, 751–767. [CrossRef]
28. Rahemi, N.; Haghighi, M.; Babaluo, A.A.; Jafari, M.F.; Khorram, S. Non-thermal plasma assisted synthesis and physicochemical characterizations of Co and Cu doped Ni/Al_2O_3 nanocatalysts used for dry reforming of methane. *Int. J. Hydrog. Energy* **2013**, *38*, 16048–16061. [CrossRef]
29. Dhal, G.C.; Dey, S.; Mohan, D.; Prasad, R. Study of Fe, Co, and Mn-based perovskite-type catalysts for the simultaneous control of soot and NOX from diesel engine exhaust. *Mater. Discov.* **2017**, *10*, 37–42. [CrossRef]
30. Li, Z.; Meng, M.; Zha, Y.; Dai, F.; Hu, T.; Xie, Y.; Zhang, J. Highly efficient multifunctional dually-substituted perovskite catalysts $La_{1-x}K_xCo_{1-y}Cu_yO_3$-δ used for soot combustion, NO_x storage and simultaneous NO_x-soot removal. *Appl. Catal. B Environ.* **2012**, *121*, 65–74. [CrossRef]
31. Dacquin, J.P.; Dujardin, C.; Granger, P. Surface reconstruction of supported Pd on $LaCoO_3$: Consequences on the catalytic properties in the decomposition of N2O. *J. Catal.* **2008**, *253*, 37–49. [CrossRef]
32. Wu, S.; Song, C.; Bin, F.; Lv, G.; Song, J.; Gong, C. $La_{1-x}Ce_xMn_{1-y}Co_yO_3$ perovskite oxides: Preparation, physico-chemical properties and catalytic activity for the reduction of diesel soot. *Mater. Chem. Phys.* **2014**, *148*, 181–189. [CrossRef]
33. Zhu, J.; Thomas, A. Perovskite-type mixed oxides as catalytic material for NO removal. *Appl. Catal. B Environ.* **2009**, *92*, 225–233. [CrossRef]
34. Leontiou, A.A.; Ladavos, A.K.; Armatas, G.S.; Trikalitis, P.N.; Pomonis, P.J. Kinetics investigation of NO + CO reaction on La–Sr–Mn–O perovskite-type mixed oxides. *Appl. Catal. A Gen.* **2004**, *263*, 227–239. [CrossRef]
35. Ladavos, A.K.; Pomonis, P.J. Mechanistic aspects of NO + CO reaction on $La_{2-x}Sr_xNiO_4$-δ (x = 0.00–1.50) perovskite-type oxides. *Appl. Catal. A Gen.* **1997**, *165*, 73–85. [CrossRef]
36. Yao, W.; Wang, R.; Yang, X. $LaCo_{1-x}Pd_xO_3$ Perovskite-Type Oxides: Synthesis, Characterization and Simultaneous Removal of NO_x and Diesel Soot. *Catal. Lett.* **2009**, *130*, 613–621. [CrossRef]
37. Wu, H.; Hu, R.; Zhou, T.; Li, C.; Meng, W.; Yang, J. A novel efficient boron-doped $LaFeO_3$ photocatalyst with large specific surface area for phenol degradation under simulated sunlight. *Cryst. Eng. Comm.* **2015**, *17*, 3859–3865. [CrossRef]
38. Xu, J.; Liu, J.; Zhao, Z.; Xu, C.; Zheng, J.; Duan, A.; Jiang, G. Easy synthesis of three dimensionally ordered macroporous $La_{1-x}K_xCoO_3$ catalysts and their high activities for the catalytic combustion of soot. *J. Catal.* **2011**, *282*, 1–12. [CrossRef]
39. Zhao, S.; Wang, L.; Wang, Y.; Li, X. Hierarchically porous $LaFeO_3$ perovskite prepared from the pomelo peel bio-template for catalytic oxidation of NO. *J. Phys. Chem. Solids* **2018**, *116*, 43–49. [CrossRef]
40. Sihaib, Z.; Puleo, F.; Pantaleo, G.; La Parola, V.; Valverde, J.L.; Gil, S.; Liotta, L.F.; Giroir-Fendler, A. The effect of citric acid concentration on the properties of $LaMnO_3$ as a catalyst for hydrocarbon oxidation. *Catalysts* **2019**, *9*, 226. [CrossRef]

41. Cai, Y.; Zhu, X.; Hu, W.; Zheng, C.; Yang, Y.; Chen, M.; Gao, X. Plasma-catalytic decomposition of ethyl acetate over $LaMO_3$ (M = Mn, Fe, and Co) perovskite catalysts. *J. Ind. Eng. Chem.* **2019**, *70*, 447–452. [CrossRef]
42. Royer, S.; Alamdari, H.; Duprez, D.; Kaliaguine, S. Oxygen storage capacity of $La_{1-x}A'_xBO_3$ perovskites (with A′ = Sr, Ce; B = Co, Mn)-relation with catalytic activity in the CH4 oxidation reaction. *Appl. Catal. B Environ.* **2005**, *58*, 273–288. [CrossRef]
43. Tarjomannejad, A.; Zonouz, P.R.; Masoumi, M.E.; Niaei, A.; Farzi, A. $LaFeO_3$ perovskites obtained from different methods for NO + CO reaction, modeling and optimization of synthesis process by response surface methodology. *J. Inorg. Organomet. Polym. Mater.* **2018**, *28*, 2012–2022. [CrossRef]
44. Ponce, S.; Peña, M.; Fierro, J.L. Surface properties and catalytic performance in methane combustion of Sr-substituted lanthanum manganites. *Appl. Catal. B Environ.* **2000**, *24*, 193–205. [CrossRef]
45. Chen, J.; Shen, M.; Wang, X.; Wang, J.; Su, Y.; Zhao, Z. Catalytic performance of NO oxidation over $LaMeO_3$ (Me = Mn, Fe, Co) perovskite prepared by the sol-gel method. *Catal. Commun.* **2013**, *37*, 105–108. [CrossRef]
46. Onrubia-Calvo, J.A.; Pereda-Ayo, B.; Cabrejas, I.; De-La-Torre, U.; González-Velasco, J.R. Ba-doped vs. Sr-doped $LaCoO_3$ perovskites as base catalyst in diesel exhaust purification. *Mol. Catal.* **2020**, *488*, 110913. [CrossRef]